



Comprehensive understanding of the active thickness in solid oxide fuel cell anodes using experimental, numerical and semi-analytical approach

Kosuke Miyawaki^{a,*}, Masashi Kishimoto^{a,b}, Hiroshi Iwai^a, Motohiro Saito^a, Hideo Yoshida^a

^a Department of Aeronautics and Astronautics, Kyoto University, Nishikyo-ku, Kyoto 615-8540, Japan

^b Department of Earth Science and Engineering, Imperial College London, London SW7 2AZ, United Kingdom

HIGHLIGHTS

- Active thickness within SOFC electrodes are investigated through numerical simulations and experiments.
- Effect of the operating conditions and microstructural parameters on the active thickness is investigated.
- The behaviour of the active thickness predicted by numerical simulation agrees well with experimental results.
- Semi-analytical descriptions are derived to identify the dominating factor for the active thickness.

ARTICLE INFO

Article history:

Received 11 February 2014

Received in revised form

18 May 2014

Accepted 20 May 2014

Available online 4 June 2014

Keywords:

Solid oxide fuel cells

Electrochemical reaction

Active thickness

Microstructure

FIB-SEM

Ni–YSZ anode

ABSTRACT

This paper reports the evaluation of the electrochemically active region in solid oxide fuel cell (SOFC) electrodes through experimental, numerical and semi-analytical approaches. In the experiment, anodes with several different thicknesses were fabricated and their performance was measured to find its dependence on the anode thickness, microstructure and operating conditions. The three-dimensional (3D) microstructure of the anodes was imaged using focused ion beam scanning electron microscopy (FIB-SEM) and the microstructural parameters were quantified. One-dimensional (1D) and 3D numerical simulations based on the actual 3D microstructures were carried out to investigate the active thickness in the anodes. The validity of the numerical models was confirmed by comparing the results with the experiment. The active thickness, i.e., the electrochemically active region within the anode, is discussed using the verified simulation models to find its dependence on various conditions. The active thickness was found to depend on the microstructure and the operating conditions. We then attempted to find a simple expression for the active thickness useful for practical applications with semi-analytical discussion. The developed descriptions expressed the quantitative dependence of the active thickness on the effective ionic conductivity, exchange current density and area-specific current density.

© 2014 Elsevier B.V. All rights reserved.

1. Introduction

Solid oxide fuel cells (SOFCs) are attracting attention for their high power generation efficiency and fuel diversity. Recently, SOFCs have been practically applied to home stationary generators and moreover, they are considered to be applicable to hybrid systems in power plants where an SOFC can be introduced into gas turbine systems. For the full-scale introduction of SOFC systems, further

research is required to improve their performance, durability and cost-effectiveness.

Ni-YSZ is commonly used as a material for SOFC porous anodes because of its low cost and high catalytic activity. The porous microstructure is composed of three phases: an electron-conductive Ni phase, an ion-conductive yttria-stabilized zirconia (YSZ) phase and a gas-diffusive pore phase. During the electrochemical reaction, various transport phenomena occur within the electrodes, i.e., ionic transport in the YSZ phase from the anode-electrolyte interface to the reaction sites, electron transport in the Ni phase from the reaction sites to the current collector and gas diffusion between the reaction sites and the electrode surface.

* Corresponding author. Tel./fax: +81 75 383 3652.

E-mail address: kosuke.miyawaki@gmail.com (K. Miyawaki).

Although the reaction sites, termed three-phase boundaries (TPBs), are distributed within the anode structure, it is widely accepted that the electrochemical reaction mostly occurs at the TPBs located in the vicinity of the anode-electrolyte interface, which is called the active reaction region or active thickness. This is because the ionic conductivity in the YSZ phase is significantly lower than the electron conductivity and gas diffusivity by several orders of magnitude. To achieve higher performance, electrodes are required to have sufficient electrochemical reaction sites in the active region as well as high conductive/diffusive flux through the three phases. Knowledge of the reaction region will therefore be significantly useful for optimizing the electrode microstructure, and hence, many researchers have attempted to identify the active thickness by both experiment and simulation [1–11].

Generally, in experimental approaches, the electrochemical performance of SOFC electrodes with several different thicknesses were evaluated by current–voltage measurement and/or electrochemical impedance spectroscopy (EIS). The reported values for the active thickness widely vary from 5 to 50 μm , which may be due to the different operating conditions and microstructures of the examined samples. In these approaches, the error caused by the individual variability of the samples is also inevitable and makes it difficult to accurately evaluate the active thickness. On the other hand, in simulation-based approaches, various methodologies have been developed to describe the porous structures and the phenomena in the electrodes. Although these approaches ensure the reproducibility of the results, few studies have discussed the validity of their models using the real electrode microstructure. To confirm the reliability of the models, results of the simulations need to be compared with experimental results.

According to the research by Kishimoto et al. [12], the active thickness is mostly determined by the balance between the oxide ion conductivity in the YSZ phase and the electrochemical reaction rate at the TPBs. Higher ionic conductivity makes it easier for ions to reach further from the electrolyte, resulting in increased active thickness. On the other hand, a higher electrochemical reaction rate enables more of the reaction to occur in the vicinity of the electrolyte, which reduces the active thickness. Since the conductivity and reaction rate are strongly affected by the electrode microstructure and operating conditions, both of them must be fully taken into account to estimate the active thickness in the electrodes.

The aim of this study is to systematically evaluate the active thickness of the anodes under various operating conditions and microstructures through both experimental and simulation-based approaches. First, the electrochemical performances of SOFC anodes are measured using anodes with various thicknesses, from which the dependence of the performance on the anode thickness is investigated. Next, the microstructural parameters are obtained through direct imaging of the anode microstructure using focused ion beam scanning electron microscopy (FIB-SEM). Subsequently, both one-dimensional (1D) and three-dimensional (3D) numerical simulations of the anodes are conducted on the basis of the actual microstructure and the results are compared with the experimental results. Finally, the active thickness is evaluated using the simulation results and then we attempt a semi-analytical approach to discover the key variables governing the active thickness.

2. Experimental

2.1. Sample preparation

In this study, Ni–YSZ cermet anodes (Ni:YSZ = 50:50 vol.%) in a button cell were examined. Fig. 1 shows a schematic picture of the prepared samples. A disk of 8 mol% YSZ (Tosoh Co., 24 mm

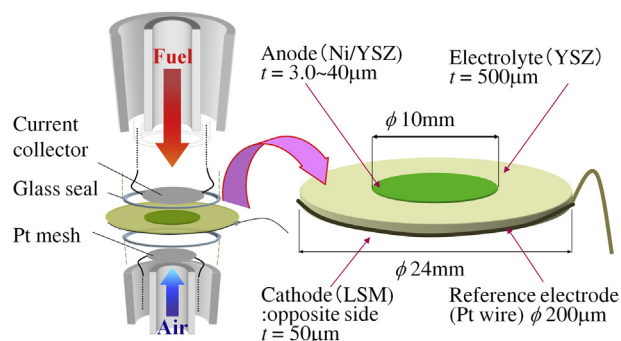


Fig. 1. Schematic picture of the single cell sample and the experimental setup.

diameter, 500 μm thickness) was used as an electrolyte. NiO powder (Wako Pure Chemical Industries, Ltd.) and YSZ powder (Tosoh Co.) were mixed and used for the anode material. The detailed procedure of the sample preparation is given in our previous works [13,14]. Here the anode material was prepared at once so as to reduce the individual difference in microstructure. In the screen printing process, several different masks were used to obtain samples with various thicknesses. Moreover, two different sintering temperatures, 1400 and 1450 $^{\circ}\text{C}$, were employed in the sintering process to obtain a series of anodes with different microstructures, which are referred hereinafter as Anode 1400 and Anode 1450, respectively. A $(\text{La}_{0.8}\text{Sr}_{0.2})_{0.97}\text{MnO}_3$ (LSM) cathode was also fabricated on the other side of the electrolyte sintered at 1150 $^{\circ}\text{C}$ for 5 h. In addition, a platinum wire (ϕ 0.2 mm) was attached around the electrolyte disk as a reference electrode.

2.2. Power generation experiment

The electrochemical characterization of the anodes was conducted with the experimental setup used in Kishimoto et al. [14]. First, the sample cell was sandwiched between alumina tubes with a Pyrex glass seal as shown in Fig. 1, and heated to 1000 $^{\circ}\text{C}$ at a heating rate of 200 $^{\circ}\text{C h}^{-1}$. Second, the temperature was kept at 1000 $^{\circ}\text{C}$ to melt the glass seal and subsequently NiO was reduced using hydrogen. Third, power generation with a potentiostatic load was conducted for at least 12 h at a terminal voltage of 0.7 V to stabilize the performance while supplying 3% H_2O –97% H_2 and 21% O_2 –79% N_2 to the anode and cathode, respectively. The total flow rate was maintained at 100 ml min^{-1} for both electrodes during the experiment. The anodic gas was humidified by bubbling hydrogen through water at a controlled temperature. Finally, the performance of the cell was measured between the anode current collector and the reference electrode at 1000 and 800 $^{\circ}\text{C}$ while supplying 3% H_2O –97% H_2 to the anode side.

2.3. Three-dimensional imaging

Microstructural information of the tested anodes was obtained using FIB-SEM. After the electrochemical characterization, the anodes were cooled down to room temperature in a reductive atmosphere and then impregnated with epoxy resin (Specifix20, Struers) under a vacuum condition at room temperature so that the pores of the anodes could be easily distinguished from solid phases during the SEM imaging. The impregnated anodes were then cut and mechanically polished for FIB-SEM imaging. In the imaging, cross-sectional images of the anode microstructure were continuously obtained using an in-lens secondary electron detector with an acceleration voltage of ~ 2 kV. From the images, we extracted

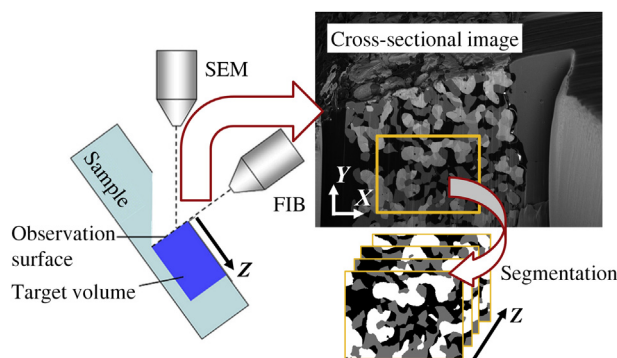


Fig. 2. Schematic picture of image acquisition and processing.

regions suitable for microstructural analysis and conducted phase segmentation based on the image brightness (Fig. 2); the Ni phase is the brightest, the pore phase is the darkest and the YSZ phase has intermediate brightness. Commercial image processing software (Avizo, Mercury Computer Systems, Inc.) was used for the phase segmentation, 3D reconstruction and some of the quantification of the microstructure. Detailed image processing procedure is as follows. First, alignment was carried out by minimizing the difference between the neighboring images. Secondly, an edge-preserving smoothing filter was applied to the images to reduce the noise, where canny filter was applied to the edge detection, followed by the Gaussian smoothing except in the detected edge region. Thirdly, the thresholding was applied to select the darkest phase, which would be segmented as the pore phase. After that the segmentation between the Ni and YSZ phases was carried out manually using the brush and blow tools implemented in the software. Mis-segmentation caused by the thresholding was also corrected manually. After the image processing, the 3D porous microstructures were reconstructed in a virtual field. In this study, orthogonal coordinate axes X and Y are embedded on the 2D SEM images and Z is the direction of the FIB milling.

From the reconstructed structures, microstructural parameters, such as volume fraction, surface-to-volume ratio, grain size, tortuosity factor and TPB density, were quantified. Volume fractions were measured by counting the number of voxels corresponding to Ni, YSZ and pore phase, and then divided by the total number of voxels in the reconstructed volume [13,15]. Surface structure was reconstructed based on the marching cube algorithm and the

surface-to-volume ratio was obtained by dividing the surface area by the total volume of the phase of interest [13]. The grain size was evaluated using the line intercept method [16,17]. The tortuosity factors were evaluated by the random-walk method [18]. The TPB density was measured using the volume expansion method [15].

3. Numerical model

To obtain the electrochemical characteristics of the electrodes, numerical simulations were conducted using the microstructural parameters obtained from the electrodes and the results were compared with those from the experiment. In this study, both a 1D model [13] and a 3D model [14] were applied to evaluate the active thickness. Both models are based on the finite volume method (FVM) and consider the conservation of electrons, ions and gas species and the electrochemical reaction at the TPBs.

3.1. Calculation domain

The calculation domains used in the 1D and 3D simulations are shown in Fig. 3. In the 1D simulation, the microstructure was assumed to be homogeneous in the entire anode volume and microstructural parameters such as the tortuosity factor, pore size and TPB density obtained previously were applied to all grids to evaluate the effective transport coefficients and the electrochemical reaction rate. On the other hand, in the 3D model, the actual structure obtained by FIB-SEM was directly used for the grid system to keep the heterogeneous information of the actual structure. The calculation domain for the 3D simulation was generated by mirroring the reconstructed structure by at most three times, and then trimmed to achieve the required thickness (4–40 μm). This mirroring extension guarantees the phase continuity across the mirroring boundaries, which is not the case in the symmetric extension. The calculation grid system were generated using the SGS model developed in our previous reports [19,20], where the structure is divided into volume elements (grids), each of which contains a number of image voxels of the FIB-SEM imaging. In each grid, the conservation of the phase volume is considered by counting the number of voxels of each phase. The heterogeneous microstructure is represented by applying the governing equations presented later at the level of the grids. Detailed information of the models is reported elsewhere [19,20]. The temperature was assumed to be constant and uniform in the anode.

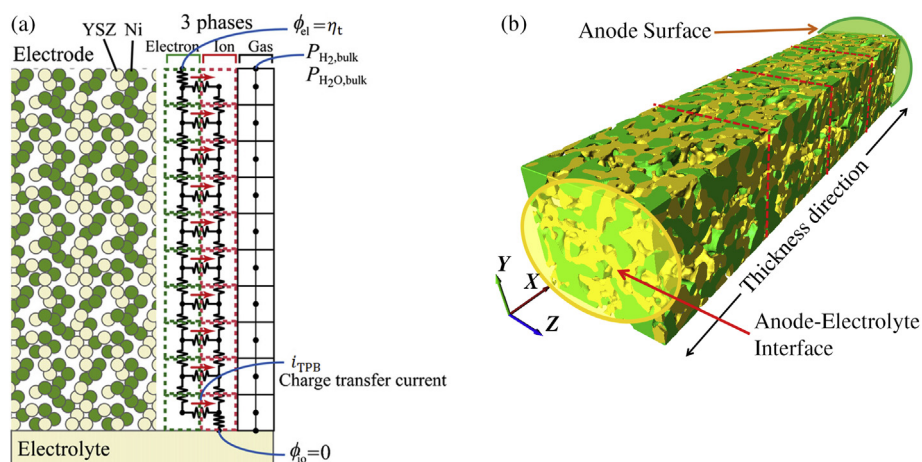


Fig. 3. Schematic picture of the calculation domains: (a) 1D model and (b) 3D model.

3.2. Governing equations

In both the 1D and 3D models, the same governing equations are solved to simulate the transport phenomena and the electrochemical reaction.

3.2.1. Electron and ion transport

In SOFC anodes, electrons and oxide ions act as charge carriers in the Ni phase and YSZ phase, respectively. The conservation of these two carriers is expressed as follows using the electric potential of the phases:

$$\nabla \cdot (\sigma_{\text{el}}^{\text{eff}} \nabla \phi_{\text{el}}) = -i_{\text{TPB}} \quad (1)$$

$$\nabla \cdot (\sigma_{\text{io}}^{\text{eff}} \nabla \phi_{\text{io}}) = i_{\text{TPB}} \quad (2)$$

where ϕ_{el} and ϕ_{io} are the electric potentials in the electron-conductive phase (Ni) and ion-conductive phase (YSZ), i_{TPB} is the density of the current exchanged between the two phases (charge-transfer current) and $\sigma_{\text{el}}^{\text{eff}}$ and $\sigma_{\text{io}}^{\text{eff}}$ are the effective electron and ion conductivities, respectively.

3.2.2. Gas diffusion

The conservation of gas species i is given by the following equation using the molar flux N_i and the source term s_i associated with the electrochemical reaction at the TPBs:

$$\nabla \cdot N_i = s_i \quad (3)$$

$$s_{\text{H}_2} = -\frac{i_{\text{TPB}}}{2F} \quad s_{\text{H}_2\text{O}} = \frac{i_{\text{TPB}}}{2F} \quad (4)$$

The dusty-gas model [21,22] is used to evaluate the diffusive flux in a multi-component gas mixture in the porous anodes:

$$\frac{N_i}{D_{i,K}^{\text{eff}}} + \sum_{j=1}^2 \frac{X_j N_i - X_i N_j}{D_{ij}^{\text{eff}}} = -\frac{P_t}{RT} \nabla X_i - \frac{X_i}{RT} \left(1 + \frac{K P_t}{\mu D_{i,K}^{\text{eff}}} \right) \nabla P_t \quad (5)$$

where X_i and N_i are the molar fraction and molar flux of gas species i , P_t is the total pressure, μ and K are the viscosity and permeability of the gas mixture and $D_{i,K}^{\text{eff}}$ and D_{ij}^{eff} are the effective Knudsen diffusion coefficients and effective binary diffusion coefficients, respectively.

In the 1D model, the effective transport coefficients Γ_i^{eff} are evaluated as follows:

$$\Gamma_i^{\text{eff}} = \frac{V_i}{\tau_i} \Gamma_i^{\text{bulk}}, \quad (6)$$

where V_i is the volume fraction, τ_i is the tortuosity factor [13], which is evaluated from the microstructure and Γ_i^{bulk} is the bulk transport coefficient [23–26]. In this study, Γ_i corresponds to the electron conductivity of the Ni phase (σ_{el}), the oxide ion conductivity of the YSZ phase (σ_{io}) or the gas diffusivities in the pore phase (D_{ij} , $D_{i,K}$).

On the other hand, in the 3D model, each grid has different volume fractions and the complexity of the structure is expressed by the distribution of the volume fractions. Therefore, the local transport coefficients $\Gamma_i^{\text{eff, local}}$ are evaluated in each grid as:

$$\Gamma_i^{\text{eff, local}} = V_i^{\text{local}} \Gamma_i^{\text{bulk}}, \quad (7)$$

where V_i^{local} is the volume fraction of phase i in the grid.

3.2.3. Electrochemical reaction

The charge-transfer current exchanged between the two solid phases is given by an empirical Butler–Volmer-like equation [27]:

$$i_{\text{TPB}} = i_0 \left[\exp\left(\frac{2F}{RT} \eta_{\text{act}}\right) - \exp\left(-\frac{F}{RT} \eta_{\text{act}}\right) \right] \quad (8)$$

where i_0 is the exchange current density. η_{act} is the activation overpotential, which is defined by the electric potential difference between the two solid phases subtracted by the concentration overpotential η_{con} :

$$\eta_{\text{act}} = \phi_{\text{el}} - \phi_{\text{io}} - \eta_{\text{con}} \quad (9)$$

$$\eta_{\text{con}} = \frac{RT}{2F} \ln \left(\frac{p_{\text{H}_2}^{\text{bulk}}}{p_{\text{H}_2}} \frac{p_{\text{H}_2\text{O}}}{p_{\text{H}_2\text{O}}^{\text{bulk}}} \right) \quad (10)$$

where $p_{\text{H}_2}^{\text{bulk}}$ and $p_{\text{H}_2\text{O}}^{\text{bulk}}$ are the gas partial pressures on the anode surface. The exchange current density i_0 is assumed to have a linear dependence on the TPB density l_{TPB} :

$$i_0 = i_{0,\text{TPB}} l_{\text{TPB}} \quad (11)$$

where $i_{0,\text{TPB}}$ is the exchange current per unit TPB length, which was obtained from the patterned anode experiments by Bieberle et al. [28,29].

$$i_{0,\text{TPB}} = 0.0013 p_{\text{H}_2}^{0.11} p_{\text{H}_2\text{O}}^{0.67} \exp\left(-\frac{0.849 \times 10^5}{RT}\right) \quad (12)$$

3.3. Boundary conditions

The boundary conditions used in both the 1D and 3D analyses are summarized in Table 1. Gas compositions were constant on the anode surface to represent the supplied fuel composition. The electric potential in the Ni phase at the anode surface and that in the YSZ phase at the anode-electrolyte interface were appropriately set so as to determine the total anode overpotential. No flux conditions were set on the anode surface for the ionic potential and on the anode-electrolyte interface for the gas components and electric potential. Additionally for the 3D simulation, no flux conditions were set on the side surfaces.

4. Results and discussion

4.1. 3D reconstruction

The thicknesses of the examined anodes were measured from the cross-sectional SEM images after the experiments. It was found that nine samples from Anode 1400 varied in thickness from ca. 3–40 μm , while those of six samples from Anode 1450 varied from ca. 5–27 μm . Fig. 4 shows the reconstructed microstructures of the anodes and Table 2 summarizes the sample sizes and voxel sizes.

Table 1
Boundary conditions.

Variables	Surface	Interface
H ₂ partial pressure	$p_{\text{H}_2} = p_{\text{H}_2}^{\text{bulk}}$	$\frac{dp_{\text{H}_2}}{dx} = 0$
H ₂ O partial pressure	$p_{\text{H}_2\text{O}} = p_{\text{H}_2\text{O}}^{\text{bulk}}$	$\frac{dp_{\text{H}_2\text{O}}}{dx} = 0$
Electric potential in Ni	$\phi_{\text{el}} = \eta_t$	$\frac{d\phi_{\text{el}}}{dx} = 0$
Electric potential in YSZ	$\frac{d\phi_{\text{io}}}{dx} = 0$	$\phi_{\text{io}} = 0$

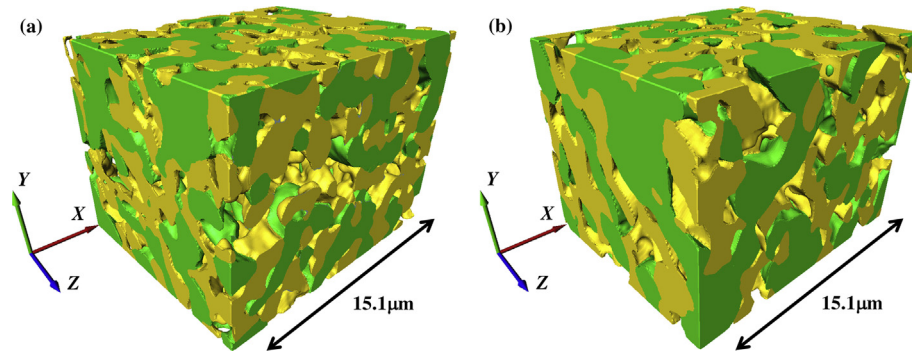


Fig. 4. Reconstructed microstructures of (a) Anode 1400 and (b) Anode 1450. (green: Ni, yellow: YSZ). (For interpretation of the references to color in this figure legend, the reader is referred to the web version of this article.)

The microstructures were successfully reconstructed with a size larger than $10^3 \mu\text{m}^3$. The quantified microstructural parameters are shown in Tables 3 and 4.

In order to guarantee the accuracy of the quantified parameters, two criteria need to be considered: (i) how many particles or pores are contained in each direction of the reconstructed volume and (ii) how many voxels are used to resolve the characteristic scale of the porous microstructure. For this purpose the results reported by Cai et al. [30] is useful; they investigated the behavior of various microstructural parameters by varying the sample volume size and the voxel size under a fixed grain size. Although the structures used in their study were synthesized structures generated by the Monte Carlo method, their findings can be used to assess the real porous microstructure. For the first criterion, given the largest characteristic scale in the two samples are found in the Ni phase, the reconstructed structures contain at least 5.75 and 4.83 particles in each direction. These are sufficient for the quantification of the volume fractions, but not for the TPB density. However, the estimated quantification error in the TPB density is not more than 10% [30], whose influence on the simulation described below is limited according to the sensitivity analysis in our previous study [31]. For the second criterion, given that the smallest grain size in this study is found in the YSZ phase, the particles are resolved by at least 19 and 15 voxels in each direction in Anode 1400 and Anode 1450, respectively. These are sufficient enough to accurately quantify the microstructural parameters [30].

However, individual variations in different samples possibly exist even within the same series of samples with the same solid volume compositions because it is difficult to fabricate electrodes with completely the same condition when the electrodes are handmade. Possible sources of the individual variations are incomplete mixing and manual screen printing process. In our previous study, we confirmed that the microstructural parameters obtained from the same fabrication procedure, but several different batches, were within reasonable error margin [15].

Although the microstructures for Anode 1400 and Anode 1450 have similar volume fractions, the grain size in Anode 1450 is ca. 20% larger, which is attributed to the higher sintering temperature

[32]. This is why the TPB density in Anode 1450 is about half of that in Anode 1400. This relation between the grain size and TPB density agrees with the work by Cai et al. [11,30]. The TPB density of Anode 1400 is similar to the value reported by Shikazono et al. [10], where the sample anodes were fabricated in the similar procedure. In addition, the surface-to-volume ratios observed in Anode 1450 are relatively smaller than those in Anode 1400, which is also because of the larger grain size. Since the percolation probabilities of the phases were found to be at least 99.5% in all phases in both samples, most of the TPBs within the electrodes are expected to be created by percolated networks.

The obtained data were implemented in the simulation models and the results will be discussed later. In the 3D simulation, the cross-sectional area perpendicular to the thickness direction (along the X axis) was $11 \mu\text{m} \times 12 \mu\text{m}$. The grid size of the generated calculation domain was $172 \text{ nm} \times 172 \text{ nm} \times 216 \text{ nm}$ for both Anode 1400 and Anode 1450. The averaged grid sizes defined as $L_{\text{grid}} = \sqrt[3]{\Delta x \Delta y \Delta z}$, where Δx , Δy and Δz are the grid sizes in each direction, were 186 nm for both samples. Given the smallest characteristic scale is found in the YSZ phase ($L_{\text{YSZ}} = 1.37$ and $1.62 \mu\text{m}$ in Anode 1400 and Anode 1450, respectively), it was resolved by 7.37 or 8.71 grid elements. This is sufficient enough for the grid system with the SGS model to give reasonable results for the overpotentials according to our previous work [19].

4.2. Experimental results and the validation of the simulation

First, the experimental results and simulation results are compared in order to discuss the validity of the simulation models. The open circuit voltage (OCV) was checked before the electrochemical measurements for all samples. It was around

Table 2
Reconstructed sample sizes and voxel sizes.

		Anode 1400	Anode 1450
Sample size [μm]	X	15.1	15.1
	Y	11.1	11.2
	Z	12.3	12.4
Voxel size [nm]	X	43.0	43.0
	Y	43.0	43.0
	Z	72.1	108

Table 3
Microstructural parameters.

Parameters	Anode 1400			Anode 1450		
	Ni	YSZ	Pore	Ni	YSZ	Pore
Volume fraction [%]	33.5	32.7	33.8	34.8	31.4	33.8
Grain size [μm]	1.93	1.37	1.79	2.32	1.62	1.90
Surface-to-volume ratio [$\mu\text{m}^2 \mu\text{m}^{-3}$]	2.85	4.45	4.32	2.27	3.49	3.69
Tortuosity factor	3.82	3.52	3.43	3.32	3.73	2.81

Table 4
TPB density.

	Anode 1400	Anode 1450
TPB density [$\mu\text{m} \mu\text{m}^{-3}$]	1.50	0.764

1.083–1.088 V for 800 °C and 1.043–1.055 V for 1000 °C for both Anode 1400 and Anode 1450. This is slightly lower than the theoretical values obtained by the Nernst equation, which are 1.101 V and 1.066 V for 800 °C and 1000 °C, respectively. The small discrepancy (~20 mV) can be attributed to the irreversible losses and imperfect sealing. EIS spectra were acquired between 0.1 Hz and 1 MHz in the experiment and Fig. 5 shows the results for an 8 μm -thick Anode 1400 at 1000 °C. Although there seems to be a single arc in the Nyquist plot, it is unclear how many physical processes construct the arcs. According to the work by Sumi et al. [33], the electrochemical reaction process appears on 1 kHz range, whereas the diffusion process appears on 1 Hz range. Therefore the impedance arcs we obtained in this study can be the sum of the activation and diffusion effects. Small distortion found in the lower frequency region is possibly the trace of the diffusion effect because it slightly expands in higher current load. Note that the diffusion effect is expected to be small in this study as the anode thickness is relatively thin and the fuel utilization is extremely low (less than 5%). From the equivalent circuit fitting analysis, it was confirmed that the inductor element, which was found to have ca. 470 nH, does not significantly alter the impedance arc, with the high-frequency intercept being shifted rightward by as small as 1 $\text{m}\Omega\text{ cm}^2$. In order to compare the simulation results with the experimental results, we defined the polarization overpotential as the sum of the activation overpotential and the concentration overpotential. Polarization resistance was evaluated from the distance between the high and low frequency intercepts in the Nyquist plot, and then multiplied by the current density to obtain the polarization overpotential, which is compared with that obtained from the numerical simulation. The definition of the polarization overpotential in the numerical simulation is found in our previous work [12].

Fig. 6 shows the overpotential characteristics of 21 μm -thick samples from Anode 1400 and Anode 1450 obtained from the experiment and the simulations. The dependence of the overpotential on the temperature is successfully reproduced by the numerical simulations. The quantitative discrepancy from the experiment may be due to the electrochemical reaction kinetic model described by Eqs. (8)–(12). For the more reliable prediction of the electrode performance, a sophisticated electrochemical model considering several elementary chemical reactions around the TPBs needs to be applied. The overpotentials predicted by the 1D model are relatively smaller than those predicted by the 3D model, which can be attributed to the homogenization method. Suppose there is an extremely narrow transport pathway (bottle neck) in a phase that could limit the transport through the phase, then the electrochemically active sites (TPBs) deep inside the structure might not be effectively used. This can be captured in the 3D model. However, when we homogenize the structure, such

effect may not be fully taken into account by the microstructural parameters because the tortuosity evaluation and the TPB evaluation are independent.

To investigate the impact of the electrode thickness on the performance, the relation between the overpotential and the anode thickness for Anode 1400 and Anode 1450 samples is analyzed (Fig. 7). Note that each plot for different thickness represents the result for a different sample in the experiment. Despite the inevitable errors that may have been caused by the individual variations of the microstructure or the inductance and other noises in the EIS measurement, the overpotential found in both the experiment and the simulation shows a noticeable drop with increasing thickness in thinner samples, while it is relatively stable in thicker samples. The active thickness is considered to be the key to explaining this result. In the region where the larger drop in the overpotential is observed, the anode thickness is considered to be less than the potential active thickness. Therefore, as the thickness increases, the anode gains more reaction sites, which leads to a smaller overpotential. In the stable region, on the other hand, where the anode thickness is greater than the active thickness, the impact of the anode thickness on the performance is less significant because the active sites are considered to be kept in the same region. Although the simulation results constantly underestimate the overpotential obtained in the experiment, they show a similar dependence on the electrode thickness; thus, we conclude that the model in this study has satisfactory sensitivity to the anode thickness and active thickness.

4.3. Evaluation of the active thickness

To evaluate the active thickness using the simulation models, we focus on the distribution of the charge-transfer current density i_{TPB} since it represents the activity of the electrochemical reaction. Fig. 8 shows distributions of the charge-transfer current in the thickness direction obtained from both 1D and 3D simulations under a constant current load of 50 mA cm^{-2} . The integral of i_{TPB} over the entire thickness corresponds to the area-specific current density; therefore, i_{TPB} obtained for thinner anodes should be larger than that for thicker anodes. This figure indicates that the effect of the electrode thickness on the reaction distribution is significant; the distribution of i_{TPB} in the thinner anodes is relatively uniform, whereas that in the thicker anodes is more concentrated in the vicinity of the anode-electrolyte interface and diminishes at the anode surface. The reason for this difference in the distribution is that the 4 and 8 μm -thick anodes are considered to be thinner than the potential active thickness; thus, most of the TPBs in the anodes are electrochemically active. The 21 and 30 μm -thick anodes, on the other hand, are considered to be thicker than the active thickness; thus, the electrochemical reaction actively occurs in the vicinity of the anode-electrolyte interface, with an electrochemically inactive region appearing in the region distant from the anode-electrolyte interface. In addition, little difference is observed between the 1D and 3D simulation results regarding the distribution of the electrochemical reaction, which suggests that the evaluation using the 1D simulation model is sufficiently reliable to discuss the distribution of the electrochemical activity.

The active thickness in this study was defined as the thickness of the region from the anode-electrolyte interface in which 90% of the electrochemical reaction occurs in a sufficiently thick anode. Since a longer computational time is required to obtain the results from the 3D simulation under various conditions, the results of the 1D simulation are used in the discussion. Fig. 9 shows the active thickness obtained from the 1D simulation with a 50 μm -thick anodes. Note that no difference was found in the active thickness when the anode thickness was increased to 100 μm because the

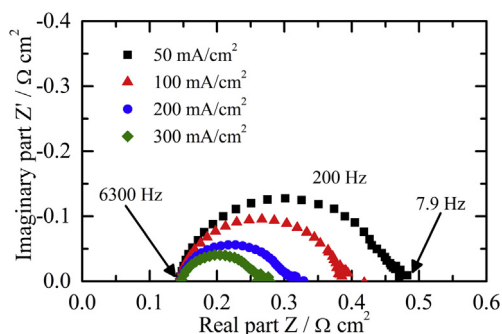


Fig. 5. Impedance spectra of Anode 1400 with 8 μm thickness measured at 1000 °C, with 3% H_2O 97% H_2 fuel supplied to the anode.

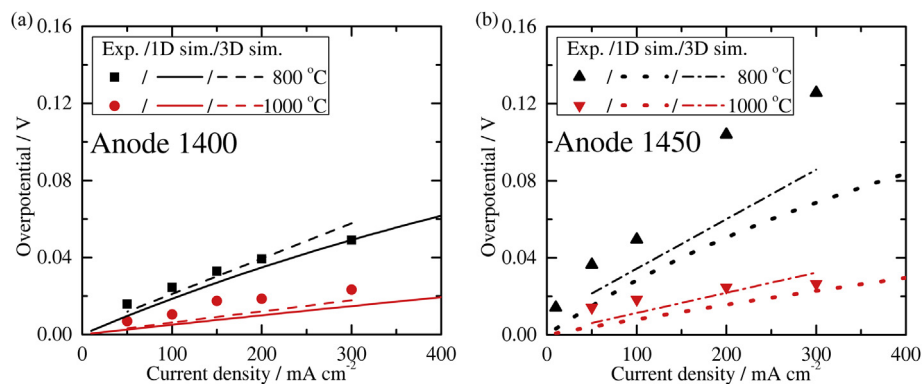


Fig. 6. The overpotential characteristics for the 21 μm -thick anode with 3% humidified hydrogen: (a) Anode 1400 and (b) Anode 1450.

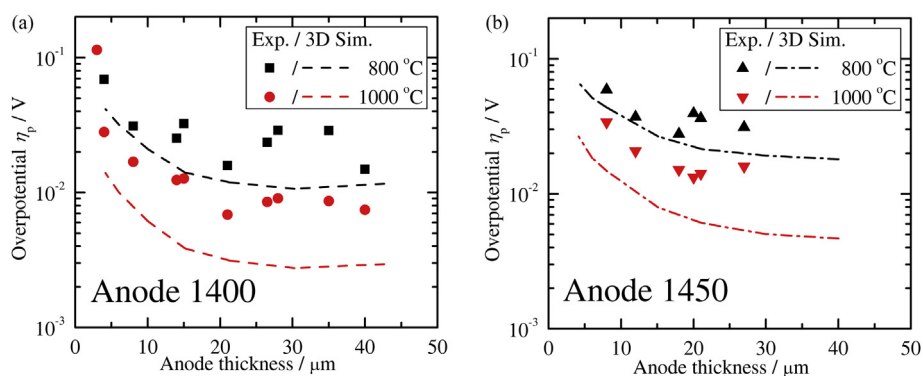


Fig. 7. Relation between anode overpotential $\bar{\eta}_p$ and anode thickness with a current density of 50 mA cm^{-2} with 3% humidified hydrogen: (a) Anode 1400 and (b) Anode 1450.

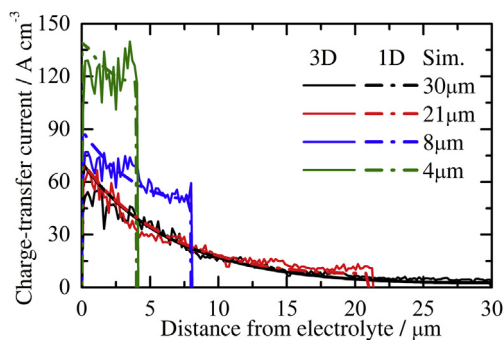


Fig. 8. Distributions of the charge-transfer current in Anode 1400 obtained by the 1D and 3D numerical simulations with a current density of 50 mA cm^{-2} at 1000°C .

active thickness within the anodes appears to be much less than $50 \mu\text{m}$ according to Fig. 8. Thus, we concluded that the active thickness in the $50 \mu\text{m}$ -thick anode only depends on the electrode microstructure and operating conditions, not on the anode thickness. The behavior of the active thickness can be explained by the ionic conductivity in the YSZ phase and the electrochemical reaction rate. When the YSZ tortuosity factor is smaller or the temperature is higher, the ionic conductivity in the YSZ phase increases and enables the transport of oxide ions further from the electrolyte, increasing the active thickness. On the other hand, a higher temperature and humidification rate or a larger TPB density enhances the reaction rate in the unit volume, enabling the consumption of more ions around the anode-electrolyte interface, which reduces the active thickness. As shown in Fig. 9(a), the active thickness is smaller at a higher humidification rate. An increase in the humidification rate enhances the reaction rate via the increase in the

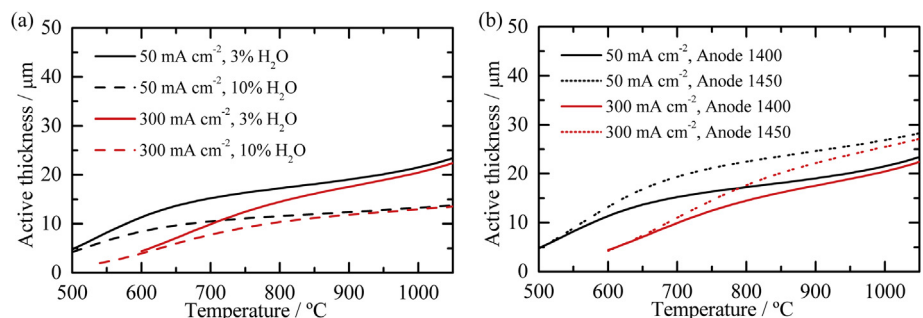


Fig. 9. The active thickness obtained from 1D simulation for (a) different humidification rate in Anode 1400 and (b) different microstructure with 3% humidified hydrogen.

exchange current density expressed as Eq. (12), resulting in a reduced active thickness. In addition, as shown in Fig. 9(b), the active thickness is generally larger in Anode 1450, which have smaller TPB density than Anode 1400. The smaller TPB density indicates less reaction sites per unit volume and it suppresses the reaction to occur around the anode-electrolyte interface, resulting in a larger active thickness. The positive correlation between the active thickness and the temperature, shown in both Fig. 9(a) and (b), suggests that the impact of an increase in the ionic conductivity is larger than that of an increase in the reaction rate. However, the correlation between the thickness and the temperature was opposite when the experimental formula obtained by de Boer [34,35] was applied for the exchange current density [12], which illustrates the importance of developing a more reliable electrochemical reaction model to precisely describe the phenomena. Moreover, a larger current density reduces the active thickness, which was also reported by Cai et al. [11]. At lower temperature, the effect of current density is more noticeable instead of that of the humidification rate and TPB density, which will be discussed later.

Following the 1D simulation results, a simple description of the active thickness is attempted by semi-analytical discussion. Kenjo et al. [36] theoretically discussed the distribution of the electrochemical reaction in a SOFC electrode based on the thin film model. The distribution of charge-transfer current found in their work can be approximated by exponentially-decaying function rather than a hyperbolic function in sufficiently thick electrode, which allows us to carry on further semi-analytical investigation on the active thickness. This description is aimed to figure out the dominating factor of the active thickness, rather than the exact match to the numerical results. The derivation of the active thickness in this study is based on the following assumptions. (i) The supplied fuel is hydrogen rich; thus, the concentration overpotential is assumed to be negligible. (ii) The distribution of the charge-transfer current in a sufficiently thick electrode can be described by the decay function.

$$i_{\text{TPB}} = \lambda \exp(-\lambda x) \quad (13)$$

Here λ is a decay factor that determines the distribution of the charge-transfer current within the electrodes, which potentially a function of the electrochemical reaction rate and the effective ionic conductivity. A smaller value of λ indicates a relatively homogeneous distribution of the electrochemical reaction, whereas a larger value indicates the localization of the reaction in the vicinity of the anode-electrolyte interface. The value of λ can be determined so as to minimize the total overpotential η_t under a certain current load. The active thickness can then be expressed using the following two descriptions depending on the electrode overpotential. Detailed procedure of the derivation is provided in Appendix.

$$l_{\text{act}} \approx 1.33 \sqrt{\frac{\sigma_{\text{io}}^{\text{eff}} RT}{Fi_0}} \quad \left(\text{at } \eta_t \ll \frac{RT}{F} \right) \quad (14)$$

$$l_{\text{act}} \approx 2.30 \frac{\sigma_{\text{io}}^{\text{eff}} RT}{FI} \quad \left(\text{at } \eta_t \gg \frac{RT}{F} \right) \quad (15)$$

The developed expressions suggest that the dependence of the active thickness is different between lower and higher overpotentials, particularly the dependence on the exchange current density i_0 and area-specific current density I . At a lower overpotential, the active thickness explicitly depends on the exchange current density. This characteristic is observed at higher temperatures in 1D simulation results (Fig. 9), where the effect of the gas composition and TPB density, which mainly determine the exchange current density, is significant. On the other hand, when the

total overpotential η_t is sufficiently large, the tendency of the active thickness can be expressed by Eq. (15), and the area-specific current density plays an important role instead of the exchange current density. This is also consistent with the result obtained at lower temperatures in 1D simulation. Figs. 10 and 11 shows the active thickness expressed by the developed functions. The dependences of the active thickness obtained from the 1D simulation, which were discussed earlier, are successfully reproduced; the active thickness is governed by the humidification rate in the higher temperature, while it depends on the area-specific current density rather than humidification rate in the lower temperature. Although there is a gap due to the approximation used in the derivation, the active thickness expressed in Eqs. (14) and (15) these formulas show both qualitative and quantitative agreement with the 1D simulation results. The agreement with the numerical simulation indicates the reliability of the developed expressions for the active thickness.

The presented expressions for the active thickness are expected to be useful for designing efficient electrodes with the optimal microstructure and thickness, particularly when the electrodes have a function layer. The optimal thickness of the function layer can be determined using the obtained insights so that the active reaction region can fit well into the function layer.

5. Conclusions

The active thickness in SOFC anodes was systematically evaluated considering various operating conditions and microstructural information using a numerical simulation model, whose validity was confirmed by a power generation experiment. In the experiment, the electrochemical performances of SOFC anodes with various electrode thicknesses were measured to evaluate the effect of the anode thickness on the anode performance. Sensitivity of the anode overpotential to the anode thickness was found to decrease as increasing the anode thickness, which evidenced the existence of the active thickness. Following the experiment, numerical simulations were conducted using the microstructural information of the examined anodes obtained using FIB-SEM. The electrode performance obtained from the simulation models showed qualitatively similar dependence on the electrode thickness to that found in the experiment. Quantitative discrepancy between the numerical simulation and the experiment can be attributed to the electrochemical reaction model employed in the models.

The active thickness of the anodes is then discussed using the 1D simulation model to evaluate the dependence of the active thickness on various conditions. The active thickness obtained from the numerical results varied from 5 to 30 μm depending on the

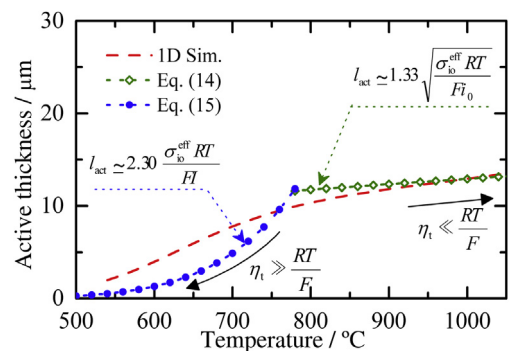


Fig. 10. The active thickness obtained from the proposed expressions (Eqs. (14) and (15)) with a current density of 300 mA cm^{-2} with 10% humidified hydrogen.

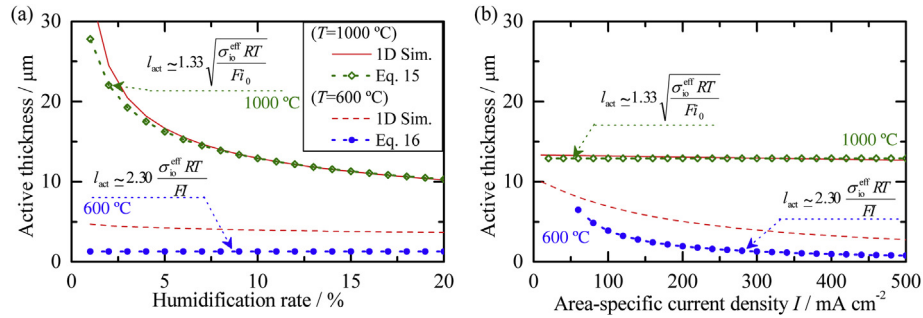


Fig. 11. Dependence of the active thickness in Anode 1400 on (a) humidification rate under a current density of 300 mA cm^{-2} and (b) area-specific current density with 10% humidified hydrogen.

conditions. The results of this study show that the low temperature, the high humidification rate and the large TPB density promotes the localization of the electrochemical reaction and decreases the active thickness. Finally, the active thickness was semi-analytically described assuming the distribution of the charge-transfer current inspired by Kenjo et al. [36]. The developed expressions successfully describe the behavior of the active thickness observed in the numerical results. They also suggest that the behavior of the active thickness is different between high and low total overpotential of the anodes.

Acknowledgments

This work was financially supported by New Energy and Industrial Technology Development Organization (NEDO) under the Development of System and Elemental Technology on Solid Oxide Fuel Cell (SOFC) Project and by Japan Society for the Promotion of Science (JSPS).

Appendix

Derivation of the active thickness

This appendix describes the semi-analytical derivation of the active thickness discussed in Section 4.3.

Charge-transfer current

To discuss the active thickness within the anodes, the distribution of the charge-transfer current density is assumed to be expressed by the following decay function (Fig. A-1):

$$i_{\text{TPB}} = C \exp(-\lambda x) \quad (0 \leq x \leq L, \lambda > 0) \quad (\text{A-1})$$

where λ is a decay constant that determines the shape of the function. A smaller value of λ indicates a relatively homogeneous distribution of the electrochemical reaction in the anode, while a larger value indicates the localization of the reaction in the vicinity of the anode-electrolyte interface.

For sufficiently thick anodes in which the charge-transfer current is sufficiently small near the anode surface, the coefficient C can be expressed as follows using the area-specific current density I loaded on the electrode:

$$I = \int_0^L i_{\text{TPB}} dx = \frac{C}{\lambda} (1 - e^{-\lambda L}) \approx \frac{C}{\lambda} \Rightarrow C \approx \lambda I \quad (\text{A-2})$$

The distribution of the charge-transfer current, or simply the decay constant λ , is determined such that the total overpotential of the anode is minimized. In this study, the total overpotential is

assumed to be the sum of the ohmic loss and activation overpotential because the contribution of the concentration overpotential and ohmic loss in the electron-conductive phase is negligible. The derivation of the ohmic loss and activation overpotential is described as follows.

Ohmic loss

Considering that the ion conductivity in the anodes is several orders of magnitude smaller than the electron conductivity, the overall ohmic loss V_{ohm} can be expressed using the local voltage drop averaged with the weight of the local charge-transfer current density as follows [37]:

$$V_{\text{ohm}} = \frac{\int_0^L \{\phi_{\text{io}}(x) - \phi_{\text{io}}(0)\} i_{\text{TPB}}(x) dx}{\int_0^L i_{\text{TPB}} dx} \quad (\text{A-3})$$

The expression $\{\phi_{\text{io}}(x) - \phi_{\text{io}}(0)\}$ can be given as follows:

$$\phi_{\text{io}}(x) - \phi_{\text{io}}(0) = \int_0^x \frac{i_{\text{io}}(x')}{\sigma_{\text{io}}^{\text{eff}}} dx' \quad (\text{A-4})$$

where i_{io} is the ionic current, which is determined by the following differential equation:

$$\frac{di_{\text{io}}(x)}{dx} = -i_{\text{TPB}}(x) \quad (i_{\text{io}}(0) = I) \quad (\text{A-5})$$

Using the expression for the charge-transfer current density given by Eq. (A-1), we obtain

$$i_{\text{io}}(x) \approx I e^{-\lambda x} \quad (\text{A-6})$$

Applying Eqs. (A-4) and (A-6) to Eq. (A-3), the ohmic loss is described as follows.

$$V_{\text{ohm}} = \frac{I}{2\lambda\sigma_{\text{io}}^{\text{eff}}} \left(1 - \frac{2e^{-\lambda L} - e^{-\lambda L}}{\lambda} \right) \approx \frac{I}{2\lambda\sigma_{\text{io}}^{\text{eff}}} \quad (\text{A-7})$$

Activation overpotential

The overall activation overpotential in the electrode is expressed as follows [37]:

$$\bar{\eta}_{\text{act}} = \frac{\int_0^L \eta_{\text{act}}(x) i_{\text{TPB}}(x) dx}{\int_0^L i_{\text{TPB}}(x) dx} \quad (\text{A-8})$$

Substitution of the integration variable is possible by using Eq. (A-1) and Butler–Volmer like equation Eq. (8) in the body of the text.

$$\begin{aligned} dx &= \frac{dx}{di_{\text{TPB}}} \frac{di_{\text{TPB}}}{d\eta_{\text{act}}} d\eta_{\text{act}} \\ &= -\frac{1}{\lambda i_{\text{TPB}}} i_0 \left[\frac{2F}{RT} \exp\left(\frac{2F}{RT} \eta_{\text{act}}\right) + \frac{F}{RT} \exp\left(-\frac{F}{RT} \eta_{\text{act}}\right) \right] d\eta_{\text{act}} \end{aligned} \quad (\text{A-9})$$

Then, Eq. (A-8) is transformed as follows:

$$\begin{aligned} \bar{\eta}_{\text{act}} &= - \int_{\eta_{\text{act}}(0)}^{\eta_{\text{act}}(L)} \eta_{\text{act}} \left\{ \frac{i_0}{\lambda} \left[\frac{2F}{RT} \exp\left(\frac{2F}{RT} \eta_{\text{act}}\right) + \frac{F}{RT} \exp\left(-\frac{F}{RT} \eta_{\text{act}}\right) \right] \right\} d\eta_{\text{act}} / \int_0^L i_{\text{TPB}}(x) dx \\ &\approx \eta_{\text{act}}(0) - \frac{i_0}{\lambda l} \frac{RT}{2F} \left\{ \exp\left(\frac{2F}{RT} \eta_{\text{act}}(0)\right) - 1 \right\} - \frac{i_0}{\lambda l} \frac{RT}{F} \left\{ \exp\left(-\frac{F}{RT} \eta_{\text{act}}(0)\right) - 1 \right\} \end{aligned} \quad (\text{A-10})$$

where $\eta_{\text{act}}(0)$ and $\eta_{\text{act}}(L)$ are the local activation overpotential at the anode-electrolyte interface and anode surface, respectively. In sufficiently thick electrodes, the value of $\eta_{\text{act}}(L)$ is zero. Equation (A-10) can be approximated as follows depending on the value of the exponent:

Applying Eq. (A-12) to Eq. (A-11), the overall activation overpotential is rewritten as follows:

$$\bar{\eta}_{\text{act}} = \begin{cases} \frac{\lambda RT l}{6F i_0} & \left(\frac{F}{RT} \eta_{\text{act}}(0) \ll 1 \right) \\ \frac{RT}{2F} \ln\left(\frac{\lambda l}{i_0}\right) + \frac{3RT i_0}{2F \lambda l} - \frac{RT}{2F} & \left(\frac{F}{RT} \eta_{\text{act}}(0) \gg 1 \right) \end{cases} \quad (\text{A-13})$$

Determination of the decay factor

On the assumption that the concentration overpotential in the anodes is negligibly small, the total overpotential η_t is written as follows:

$$\eta_t = \begin{cases} \frac{I}{2\lambda \sigma_{io}^{\text{eff}}} + \frac{\lambda RT l}{6F i_0} & \left(\frac{F}{RT} \eta_{\text{act}}(0) \ll 1 \right) \\ \frac{I}{2\lambda \sigma_{io}^{\text{eff}}} + \frac{RT}{2F} \ln\left(\frac{\lambda l}{i_0}\right) + \frac{3RT i_0}{2F \lambda l} - \frac{RT}{2F} & \left(\frac{F}{RT} \eta_{\text{act}}(0) \gg 1 \right) \end{cases} \quad (\text{A-14})$$

$$\bar{\eta}_{\text{act}} \approx \begin{cases} \eta_{\text{act}}(0) - \frac{3i_0}{2\lambda l} \frac{F}{RT} \eta_{\text{act}}(0)^2 & \left(\frac{F}{RT} \eta_{\text{act}}(0) \ll 1 \right) \\ \eta_{\text{act}}(0) - \frac{i_0}{\lambda l} \frac{RT}{2F} \left\{ \exp\left(\frac{2F}{RT} \eta_{\text{act}}(0)\right) - 1 \right\} + \frac{i_0}{\lambda l} \frac{RT}{F} & \left(\frac{F}{RT} \eta_{\text{act}}(0) \gg 1 \right) \end{cases} \quad (\text{A-11})$$

The relation between the local activation overpotential η_{act} and the charge-transfer current density in the SOFC electrodes, expressed by a Butler–Volmer-like equation, is often approximated by the following linear relationship or Tafel equation depending on the value of the exponent in Eq. (9):

Since the electrode is considered to have the distribution of charge-transfer current that minimizes the total overpotential, the decay factor must satisfy $\partial \eta_t / \partial \lambda = 0$ and is determined as follows:

$$\eta_{\text{act}}(0) \approx \begin{cases} \frac{RT}{3F i_0} i_{\text{TPB}}(0) = \frac{RT \lambda l}{3F i_0} & \left(\frac{F}{RT} \eta_{\text{act}}(0) \ll 1 \right) \\ \frac{RT}{2F} \ln\left(\frac{i_{\text{TPB}}(0)}{i_0}\right) = \frac{RT}{2F} \ln\left(\frac{\lambda l}{i_0}\right) & \left(\frac{F}{RT} \eta_{\text{act}}(0) \gg 1 \right) \end{cases} \quad (\text{A-12})$$

$$\lambda = \begin{cases} \sqrt{\frac{3F i_0}{\sigma_{io}^{\text{eff}} RT}} & \left(\frac{F}{RT} \eta_{\text{act}}(0) \ll 1 \right) \\ \frac{F l}{\sigma_{io}^{\text{eff}} RT} + \frac{3i_0}{l} & \left(\frac{F}{RT} \eta_{\text{act}}(0) \gg 1 \right) \end{cases} \quad (\text{A-15})$$

$$\eta_t = \begin{cases} \sqrt{\frac{RTI^2}{3F\sigma_{io}^{eff}i_0}} & \left(\frac{F}{RT}\eta_{act}(0) \ll 1\right) \\ \frac{RT}{2F} \ln\left(\frac{FI^2}{\sigma_{io}^{eff}RTi_0} + 3\right) & \left(\frac{F}{RT}\eta_{act}(0) \gg 1\right) \end{cases} \quad (A-16)$$

Applying Eq. (A-15) to Eq. (A-12), we obtain $\eta_{act}(0) = \eta_t$.

Active thickness

The active thickness l_{act} is defined as the thickness of the region from the electrolyte in which 90% of the reaction occurs and is expressed as follows:

$$\int_0^l i_{TPB} dx = 0.9I \Rightarrow l_{act} = \frac{\ln 10}{\lambda} \quad (A-17)$$

Applying Eq. (A-15) to Eq. (A-17), the active thickness can be obtained in the following form:

$$l_{act} = \sqrt{\frac{\sigma_{io}^{eff}RT}{3Fi_0}} \ln 10 \approx 1.33 \sqrt{\frac{\sigma_{io}^{eff}RT}{Fi_0}} \left(\frac{F}{RT}\eta_t \ll 1\right) \quad (A-18)$$

$$\begin{aligned} l_{act} &= \frac{\ln 10}{\frac{FI}{\sigma_{io}^{eff}RT} + 3\frac{i_0}{I}} \\ &= \frac{\sigma_{io}^{eff}RT}{FI} \left(1 - 3 \exp\left(-\frac{2F}{RT}\eta_t\right)\right) \ln 10 \quad \left(\frac{F}{RT}\eta_t \gg 1\right) \end{aligned} \quad (A-19)$$

When the value of $F/RT\eta_t$ is sufficiently large, the active thickness expressed by Eq. (A-19) approaches Eq. (A-20).

$$l_{act} \approx \frac{\sigma_{io}^{eff}RT}{FI} \ln 10 \approx 2.30 \frac{\sigma_{io}^{eff}RT}{FI} \quad (A-20)$$

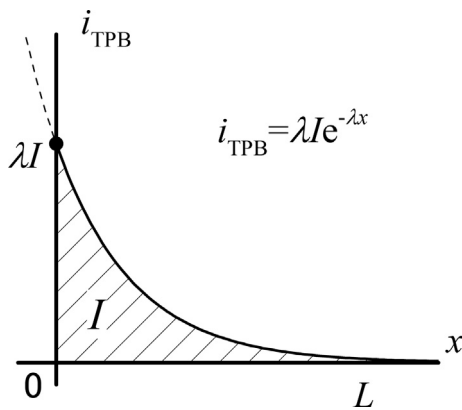


Fig. A-1. Schematic picture of the charge-transfer current density assumed in the derivation of the active thickness.

Nomenclature

D	diffusion coefficient, $m^2 s^{-1}$
F	Faraday constant, $C mol^{-1}$
I	area-specific current density, $A m^{-2}$
$i_{0,TPB}$	exchange current per unit TPB length, $A m^{-1}$
K	permeability, m^2

L	anode thickness, m
l_{act}	active thickness, m
l_{TPB}	TPB density, $m m^{-3}$
M	molar weight, $kg mol^{-1}$
N	molar flux, $mol m^{-2} s^{-1}$
P	partial pressure, Pa
R	gas constant, $J mol^{-1} K^{-1}$
T	temperature, K
V	volume fraction
X	molar ratio

Greek symbols

η	overpotential, V
$\bar{\eta}$	averaged overpotential, V
λ	decay factor, m^{-1}
μ	viscosity, Pa s
σ	conductivity, $S m^{-1}$
$\sum v$	diffusion volume, m^3
τ	tortuosity factor
ϕ	electric potential, V
Γ	general transport coefficient

Subscripts

act	activation
bulk	bulk fluid
con	concentration
el	electron
H_2	hydrogen
H_2O	steam
io	ion
K	Knudsen
O_2	oxygen
t	total
TPB	three-phase boundary
0	standard state

Superscripts

eff	effective value in porous medium
-----	----------------------------------

References

- [1] M. Juhl, S. Prindahl, C. Manon, M. Mogensen, J. Power Sources 61 (1996) 173–181.
- [2] K. Chen, X. Chen, Z. Lu, N. Ai, X. Huang, W. Su, Electrochim. Acta 53 (2008) 7825–7830.
- [3] S. Prindahl, M. Mogensen, J. Electrochem. Soc. 144 (1997) 3409–3419.
- [4] J. Kong, K. Sun, D. Zhou, N. Zhang, J. Mu, J. Qiao, J. Power Sources 166 (2007) 337–342.
- [5] H. Moon, S.D. Kim, E.W. Park, S.H. Hyun, H.S. Kim, Int. J. Hydrogen Energy 33 (2008) 2826–2833.
- [6] M. Brown, S. Prindahl, M. Mogensen, J. Electrochem. Soc. 147 (2) (2000) 475–485.
- [7] S. Sunde, J. Electrochem. Soc. 143 (1996) 1930–1939.
- [8] S.H. Chan, Z.T. Xia, J. Electrochem. Soc. 148 (2001) A388–A394.
- [9] K. Yuan, Y. Ji, J.N. Chung, J. Power Sources 194 (2009) 908–919.
- [10] N. Shikazono, D. Kanno, K. Matsuzaki, H. Teshima, S. Sumino, N. Kasagi, J. Electrochem. Soc. 157 (2010) B665–B672.
- [11] Q. Cai, C.S. Adjiman, N.P. Brandon, Electrochim. Acta 56 (2011) 10809–10819.
- [12] M. Kishimoto, H. Iwai, M. Saito, H. Yoshida, ECS Trans. 57 (1) (2013) 2515–2525.
- [13] M. Kishimoto, H. Iwai, M. Saito, H. Yoshida, J. Power Sources 196 (2011) 4555–4563.
- [14] M. Kishimoto, H. Iwai, K. Miyawaki, M. Saito, H. Yoshida, Fuel Cells 13 (4) (2013) 476–486.
- [15] H. Iwai, N. Shikazono, T. Matsui, H. Teshima, M. Kishimoto, R. Kishida, D. Hayashi, K. Matsuzaki, D. Kanno, M. Saito, H. Muroyama, K. Eguchi, N. Kasagi, H. Yoshida, J. Power Sources 195 (2010) 955–961.
- [16] D. Simwonis, F. Tietz, D. Stöver, Solid State Ionics 132 (2000) 241–251.
- [17] J.H. Lee, H. Moon, H.W. Lee, J. Kim, J.D. Kim, K.H. Yoon, Solid State Ionics 148 (2002) 15–26.
- [18] Y. Nakashima, S. Kamiya, J. Nucl. Sci. Technol. 44 (9) (2007) 1233–1247.

- [19] M. Kishimoto, H. Iwai, M. Saito, H. Yoshida, J. Electrochem. Soc. 159 (2012) B315–B323.
- [20] M. Kishimoto, H. Iwai, K. Miyawaki, M. Saito, H. Yoshida, J. Power Sources 223 (2013) 268–276.
- [21] E.A. Mason, A.P. Malinauskas, R.B. Evans III, J. Chem. Phys. 46 (8) (1967) 3199–3216.
- [22] D. Arnošt, P. Schneider, Chem. Eng. J. 57 (1995) 91–99.
- [23] U. Anselmi-Tamburini, G. Chiodelli, M. Arimondi, F. Maglia, G. Spinolo, Z.A. Munir, Solid State Ionics 110 (1998) 35–43.
- [24] N.F. Bessette II, W.J. Wepfer, J. Winnick, J. Electrochem. Soc. 142 (11) (1995) 3792–3800.
- [25] A.V. Akkaya, Int. J. Energy Res. 31 (2007) 79–98.
- [26] E.N. Fuller, P.D. Schettler, J.C. Giddings, Ind. Eng. Chem. Res. 58 (5) (1966) 18–27.
- [27] T. Kawada, N. Sakai, H. Yokokawa, M. Dokiya, M. Mori, T. Iwata, J. Electrochem. Soc. 137 (10) (1990) 3042–3047.
- [28] A. Bieberle, L.P. Meier, L.J. Gauckler, J. Electrochem. Soc. 148 (6) (2001) A646–A656.
- [29] D. Kanno, N. Shikazono, N. Takagi, K. Matsuzaki, N. Kasagi, Electrochim. Acta 56 (2011) 4015–4021.
- [30] Q. Cai, C.S. Adjiman, N.P. Brandon, Electrochim. Acta 56 (2011) 5804–5814.
- [31] M. Kishimoto, H. Iwai, M. Saito, H. Yoshida, in: Proceedings of the 14th Int. Heat Trans. Conf. IHTC14-22495.
- [32] J. Sehested, J.A.P. Gelten, S. Helveg, Appl. Catal. A: Gen. 309 (2) (2006) 237–246.
- [33] H. Sumi, T. Yamaguchi, K. Hamamoto, T. Suzuki, Y. Fujihiro, T. Matsui, K. Eguchi, Electrochim. Acta 67 (2012) 159–165.
- [34] B. de Boer, Ph.D. Thesis, University of Twente, 1998.
- [35] Y. Suzue, N. Shikazono, N. Kasagi, J. Power Sources 184 (2008) 52–59.
- [36] T. Kenjo, S. Osawa, K. Fujikawa, J. Electrochem. Soc. 138 (1991) 349–355.
- [37] A. Konno, H. Iwai, M. Saito, H. Yoshida, Heat Transf. Asian Res. 41 (2012) 700–718.